JOURNAL OF COMPUTATIONAL PHYSICS 86, 270–293 (1990)

Compressible Linear and Nonlinear Resistive MHD Calculations in Toroidal Geometry*

L. A. CHARLTON, J. A. HOLMES, V. E. LYNCH, AND B. A. CARRERAS

Oak Ridge National Laboratory, P. O. Box 2009,
Oak Ridge, Tennessee 37831

AND

T. C. HENDER

Euratom/UKAEA Fusion Association, Culham Laboratory, Abingdon,
Oxon OX14 3DB, England

Received September 19, 1988; revised February 27, 1989

A formalism has been developed and incorporated in the computer code FAR to solve the magnetohydrodynamic (MHD) equations compressibly or incompressibly for either ideal or resistive modes. A linear subset or the full nonlinear set of equations can be solved, in toroidal geometry, with no ordering assumptions. Significant features of the formalism include (1) the addition of compressibility by adding two equations to a basic incompressible set, (2) the ability of the code to converge very rapidly for linear calculations, and (3) the use of a diffusive term in the evaluation of the compressible part of the velocity. This term damps the short-wavelength waves and allows a time step size which is comparable to that needed for incompressible simulations. © 1990 Academic Press, Inc.

1. INTRODUCTION

Because of the complexity of the problem, MHD calculations in toroidal geometry are usually done with some simplifying assumptions. Although exceptions exist [1], these calculations frequently involve the use of reduced [2] or ideal [3] equations or an incompressibility assumption [4]. The reduced equations neglect the toroidal components of the perturbation and thus allow a significant reduction in the complexity of the equations to be solved. Neglecting resistive effects casts the problem in a form involving a self-adjoint operator, which allows the use of a δW approach. In a time evolution approach, incompressibility reduces the number of equations to be time-advanced by two since the time-independent incompressibility

---

* Research sponsored by the Office of Fusion Energy, U.S. Department of Energy, under Contract DE-AC05-84OR21400 with Martin Marietta Energy Systems, Inc. The U.S. Government's right to retain a nonexclusive royalty-free license in and to the copyright covering this paper, for governmental purposes; is acknowledged.

0021-9991/90 $3.00

assumption serves as one equation and the equations can be cast in a form that does not explicitly require a pressure. In this paper, we report a method for solving the full MHD equations with resistivity and in toroidal geometry which uses none of the preceding approximations and which has been implemented in the computer code FAR.

First, the equations used are developed in Section 2, and the numerical method is described in Section 3. The boundary conditions are discussed in Section 4, and the relaxation of the strict nonlinear compressible time step restrictions is considered in Section 5. Results are given in Section 6, and the discussion and conclusions, in Section 7.

2. EQUATIONS

We begin with the usual MHD equations, namely (in mks units),

$$\frac{\partial \mathbf{B}}{\partial t} = \nabla \times \mathbf{E}, \tag{1}$$

$$\mathbf{E} + \mathbf{V} \times \mathbf{B} = \eta \mathbf{J}, \tag{2}$$

$$\rho_m \left(\frac{\partial \mathbf{V}}{\partial t} + \mathbf{V} \cdot \nabla \mathbf{V} \right) = -\nabla p + \mathbf{J} \times \mathbf{B}, \tag{3}$$

$$\mu_0 \mathbf{J} = \nabla \times \mathbf{B}, \tag{4}$$

$$\nabla \cdot \mathbf{B} = 0, \tag{5}$$

and an equation of state can be chosen to satisfy either incompressible ($\nabla \cdot \mathbf{V} = 0$) or compressible ($\nabla \cdot \mathbf{V} \neq 0$) model assumptions. For the compressible model, a pressure evolution equation is used,

$$\frac{\partial p}{\partial t} = -\mathbf{V} \cdot \nabla p - \Gamma \nabla \cdot \mathbf{V}, \tag{6}$$

where Γ is the ratio of specific heats. The incompressible equation of state is specified later by Eq. (15).

In our formulation the magnetic field is written in terms of the usual vector potential ($\mathbf{A}$) as

$$\mathbf{B} = \nabla \times \mathbf{A}; \tag{7}$$

the velocity is expressed as a sum of compressible and incompressible parts as

$$\mathbf{V} = \nabla \times \mathbf{\Omega} + \nabla \omega; \tag{8}$$

and the mass density (ρ_m) is taken to be a constant. The preceding specification of the velocity would seem to overspecify the velocity since a three-component vector

($\mathbf{\Omega}$) and a scalar (ω) are being used. However, a gaugelike choice is made after specification of the coordinate system, which will remove the apparent overspecification.

From Eqs. (1), (2), and (7), we find that

$$\frac{\partial \mathbf{A}}{\partial t} = \mathbf{V} \times \mathbf{B} - \eta \mathbf{J} + \nabla \alpha, \tag{9}$$

where α is the electrostatic potential.

Taking the curl and divergence of Eq. (3) allows the velocity evolution equations to be divided into incompressible,

$$\frac{\partial \mathbf{U}}{\partial t} = \nabla \times (\mathbf{V} \times \mathbf{U}) + \frac{1}{\rho_m} \nabla \times (\mathbf{J} \times \mathbf{B}), \tag{10}$$

and compressible,

$$\begin{aligned}\frac{\partial W}{\partial t} = {} & -\frac{1}{2} \nabla^2 V^2 + \nabla \cdot (\mathbf{V} \times \mathbf{U}) \\ & -\frac{1}{\rho_m} \nabla^2 p + \frac{1}{\rho_m} \nabla \cdot (\mathbf{J} \times \mathbf{B}),\end{aligned} \tag{11}$$

parts, where

$$W = \nabla \cdot \mathbf{V} = \nabla^2 \omega \tag{12}$$

and

$$\mathbf{U} = \nabla \times \mathbf{V} = \nabla \times (\nabla \times \mathbf{\Omega}). \tag{13}$$

Although Eq. (10) has the form of a vector equation, only two of the components are independent since

$$\nabla \cdot \mathbf{U} = \nabla \cdot (\nabla \times \mathbf{V}) = 0 \tag{14}$$

can be used to specify the third component. Still to be specified is the choice of gauge for the magnetic field and the effective choice of gauge for the velocity field. This is done below. For the incompressible mode, $(\partial/\partial t)(\nabla \cdot \mathbf{V}) = 0$, which gives the effective equation of state as

$$\nabla^2 p = \nabla \cdot (\mathbf{J} \times \mathbf{B}) - \frac{\rho_m}{2} \nabla^2 V^2 + \rho_m \nabla \cdot (\mathbf{V} \times \mathbf{U}). \tag{15}$$

Thus, for incompressible calculations, Eqs. (9) and (10) are solved with Eq. (15) specifying the pressure (as a diagnostic). In addition, for compressible calculations, Eq. (11) gives the compressible part of the velocity evolution, and Eq. (6) defines the evolution of the pressure. The use of an ideal equation of state is not consistent with energy conservation since ohmic heating is neglected. The resistivity (η) is assumed time independent and is specified by the inverse of the flux surface average of the toroidal equilibrium current density. No explicit external electric field is imposed. However, the purely equilibrium resistive terms are dropped which could be viewed as the imposition of an electric field.

A nonorthogonal coordinate system is used which is based on the toroidal equilibrium configuration [7] with coordinates ρ, θ, and ζ [8]. An equilibrium flux surface is labeled by ρ, the poloidal anglelike variable θ is chosen so that the equilibrium magnetic field lines are straight, and the geometric toroidal angle is ζ. With this definition of the coordinate system, the gauge can now be specified and is chosen to be

$$A_\rho = 0, \tag{16}$$

with a similar gaugelike constraint on the velocity

$$\Omega_\rho = 0. \tag{17}$$

Additional details of the coordinate system are given in Ref. [8].

With the preceding specifications and the definitions $A_\zeta = -\psi$ (the poloidal magnetic flux function), $A_\theta = -\chi$ (the toroidal magnetic flux function), $\Omega_\zeta = -\phi$ (the poloidal stream function), and $\Omega_\theta = -\Lambda$ (the toroidal stream function), the equations that are solved are (in dimensionless form):

$$\frac{\partial \alpha}{\partial \rho} = -\frac{1}{R^2}\,(V^\theta B^\zeta - V^\zeta B^\theta) + \eta J_\rho, \tag{18}$$

$$\frac{\partial \chi}{\partial t} = -\frac{1}{R^2}\,(V^\zeta B^\rho - V^\rho B^\zeta) + \eta J_\theta - \frac{1}{\rho}\frac{\partial}{\partial \theta}\,\alpha, \tag{19}$$

$$\frac{\partial \psi}{\partial t} = -\frac{1}{R^2}\,(V^\rho B^\theta - V^\theta B^\rho) + \eta J_\zeta - \frac{\partial}{\partial \zeta}\,\alpha, \tag{20}$$

$$\begin{aligned}\frac{\partial U^\theta}{\partial t} = {}& \frac{\partial}{\partial \zeta}\left\{\frac{1}{R^2}\,[S^2(J^\theta B^\zeta - J^\zeta B^\theta) - (U^\theta V^\zeta - U^\zeta V^\theta)]\right\} \\ & - \frac{\partial}{\partial \rho}\left\{\frac{1}{R^2}\,[S^2(J^\rho B^\theta - J^\theta B^\rho) - (U^\rho V^\theta - U^\theta V^\rho)]\right\},\end{aligned} \tag{21}$$

$$\begin{aligned}\frac{\partial U^\zeta}{\partial t} = {}& \frac{1}{\rho}\frac{\partial}{\partial \rho}\left\{\frac{\rho}{R^2}\,[S^2(J^\zeta B^\rho - J^\rho B^\zeta) - (U^\zeta V^\rho - U^\rho V^\zeta)]\right\} \\ & - \frac{1}{\rho}\frac{\partial}{\partial \theta}\left\{\frac{1}{R^2}\,[S^2(J^\theta B^\zeta - J^\zeta B^\theta) - (U^\theta V^\zeta - U^\zeta V^\theta)]\right\},\end{aligned} \tag{22}$$

$$\begin{aligned}\frac{\partial W}{\partial t} = & -\frac{1}{2}\,\nabla^2\mathbf{V}^2 + \frac{1}{\rho}\,\frac{\partial}{\partial\rho}\left\{\frac{\rho}{R^2}\,[S^2(J_\theta B_\zeta - J_\zeta B_\theta) - (U_\theta V_\zeta - U_\zeta V_\theta)]\right\} \\ & + \frac{1}{\rho}\,\frac{\partial}{\partial\theta}\left\{\frac{1}{R^2}\,[S^2(J_\zeta B_\rho - J_\rho B_\zeta) - (U_\zeta V_\rho - U_\rho V_\zeta)]\right\} \\ & + \frac{\partial}{\partial\zeta}\left\{\frac{1}{R^2}\,[S^2(J_\rho B_\theta - J_\theta B_\rho) - (U_\rho V_\theta - U_\theta V_\rho)]\right\} - \frac{S^2\beta_0}{2\varepsilon^2}\,\nabla^2 p \\ & + D_A \nabla_\perp^2 W, \end{aligned} \tag{23}$$

$$\begin{aligned}\frac{\partial p}{\partial t} = & -\frac{1}{R^2}\left(V^\rho\,\frac{\partial p}{\partial\rho} + V^\theta\,\frac{1}{\rho}\,\frac{\partial p}{\partial\theta} + V^\zeta\,\frac{\partial p}{\partial\zeta}\right) \\ & -\frac{\Gamma p}{R^2}\left[\frac{1}{\rho}\,\frac{\partial}{\partial\rho}\,(\rho V^\rho) + \frac{1}{\rho}\,\frac{\partial}{\partial\theta}\,V^\theta + \frac{\partial}{\partial\zeta}\,V^\zeta\right], \end{aligned} \tag{24}$$

where

$$\mathbf{V}^2 = \frac{1}{R^4}\,(V^\rho V_\rho + V^\theta V_\theta + V^\zeta V_\zeta) \tag{25}$$

and

$$\begin{aligned}\nabla^2 = & \frac{1}{\rho}\,\frac{\partial}{\partial\rho}\left(\rho g^{\rho\rho} R^2\,\frac{\partial}{\partial\rho}\right) + \frac{1}{\rho}\,\frac{\partial}{\partial\rho}\left(\rho g^{\rho\theta} R^2\,\frac{1}{\rho}\,\frac{\partial}{\partial\theta}\right) \\ & + \frac{1}{\rho}\,\frac{\partial}{\partial\theta}\left(g^{\rho\theta} R^2\,\frac{\partial}{\partial\rho}\right) + \frac{1}{\rho}\,\frac{\partial}{\partial\theta}\left(g^{\theta\theta} R^2\,\frac{1}{\rho}\,\frac{\partial}{\partial\theta}\right) \\ & + \varepsilon^2\,\frac{\partial}{\partial\zeta}\left(g^{\zeta\zeta} R^2\,\frac{\partial}{\partial\zeta}\right). \end{aligned} \tag{26}$$

$\nabla_\perp^2$ in Eq. (23) is equal to ∇^2 above with the toroidal terms omitted.

The vector components of the magnetic field are given by

$$B^\rho = \frac{\partial}{\partial\zeta}\,\chi - \frac{1}{\rho}\,\frac{\partial}{\partial\theta}\,\psi, \tag{27}$$

$$B^\theta = \frac{\partial}{\partial\rho}\,\psi, \tag{28}$$

$$B^\zeta = -\frac{1}{\rho}\,\frac{\partial(\rho\chi)}{\partial\rho}, \tag{29}$$

and the current density components are

$$J^{\rho} = -\left\{\frac{1}{\varepsilon^2}\frac{1}{\rho}\frac{\partial}{\partial\theta}\left[\frac{1}{\rho}\frac{\partial}{\partial\rho}(\rho\chi)\right] - \frac{1}{\rho}\frac{\partial}{\partial\zeta}\left[g^{\rho\theta}\frac{\partial(\rho\chi)}{\partial\zeta}\right]\right\}$$
$$-\left[\frac{\partial}{\partial\zeta}\left(\frac{g^{\rho\theta}}{\rho}\frac{\partial\psi}{\partial\theta}\right) + \frac{\partial}{\partial\zeta}\left(g^{\rho\rho}\frac{\partial\psi}{\partial\rho}\right)\right], \tag{30}$$

$$J^{\theta} = -\left\{-\frac{\partial}{\partial\zeta}\left[\frac{1}{\rho}g^{\theta\theta}\frac{\partial}{\partial\zeta}(\rho\chi)\right] - \frac{1}{\varepsilon^2}\frac{\partial}{\partial\rho}\left[\frac{1}{\rho}\frac{\partial}{\partial\rho}(\rho\chi)\right]\right\}$$
$$-\left[\frac{\partial}{\partial\zeta}\left(\frac{g^{\theta\theta}}{\rho}\frac{\partial\psi}{\partial\theta}\right) + \frac{\partial}{\partial\zeta}\left(g^{\rho\theta}\frac{\partial\psi}{\partial\rho}\right)\right], \tag{31}$$

$$J^{\zeta} = -\left\{\frac{1}{\rho}\frac{\partial}{\partial\rho}\left[g^{\rho\theta}\frac{\partial}{\partial\zeta}(\rho\chi)\right] + \frac{1}{\rho^2}\frac{\partial}{\partial\theta}\left[g^{\theta\theta}\frac{\partial}{\partial\zeta}(\rho\chi)\right]\right\}$$
$$-\left[-\frac{1}{\rho}\frac{\partial}{\partial\rho}\left(g^{\rho\theta}\frac{\partial\psi}{\partial\theta}\right) - \frac{1}{\rho}\frac{\partial}{\partial\rho}\left(\rho g^{\rho\rho}\frac{\partial\psi}{\partial\rho}\right)\right.$$
$$\left.-\frac{1}{\rho}\frac{\partial}{\partial\theta}\left(g^{\theta\theta}\frac{1}{\rho}\frac{\partial}{\partial\theta}\psi\right) - \frac{1}{\rho}\frac{\partial}{\partial\theta}\left(g^{\rho\theta}\frac{\partial}{\partial\rho}\psi\right)\right]. \tag{32}$$

The three components of the velocity are given by

$$V^{\rho} = R^2\left(g^{\rho\rho}\frac{\partial\omega}{\partial\rho} + g^{\rho\rho}\frac{1}{\rho}\frac{\partial\omega}{\partial\theta}\right) + \frac{\partial A}{\partial\zeta} - \frac{1}{\rho}\frac{\partial\phi}{\partial\theta}, \tag{33}$$

$$V^{\theta} = R^2\left(g^{\rho\theta}\frac{\partial\omega}{\partial\rho} + g^{\theta\theta}\frac{1}{\rho}\frac{\partial\omega}{\partial\theta}\right) + \frac{\partial\phi}{\partial\rho}, \tag{34}$$

$$V^{\zeta} = \varepsilon^2\frac{\partial\omega}{\partial\zeta} - \frac{1}{\rho}\frac{\partial(\rho A)}{\partial\rho}. \tag{35}$$

The components of the vorticity are defined as the current density with A replacing χ and ϕ replacing ψ.

In Eqs. (18)–(35), all lengths are normalized to a generalized minor radius a (defined by $a^2 = R_0 \int R^{-2}\, dV/(2\pi^2)$, with integration over the plasma volume). The resistivity is normalized to η_0 (its value at the magnetic axis); the time, to the resistive diffusion time $\tau_r = a^2\mu_0/\eta_0$, where μ_0 is the vacuum magnetic permeability; the magnetic field, to B_0 (the toroidal vacuum field at the plasma major radius R_0); the velocity, to a/τ_r; and the pressure, to p_0 (its equilibrium value at the magnetic axis). R is the major radius coordinate normalized to R_0, and $S = \tau_r/\tau_{HP}$ is the ratio of the resistive time to the poloidal Alfvén time $[\tau_{HP} = R_0(\mu_0\rho_m)^{1/2}/B_0]$. The quantities β_0 and ε are given by $\beta_0 = p_0(0)/(B_0^2/2\mu_0)$ and $\varepsilon = a/R_0$. In Eq. (23), a term $(D_A\nabla_\perp^2\omega)$ has been added, which is discussed later (D_A is normalized to a^2/τ_r).

The above equations are solved by initializing with an equilibrium, perturbing it, and following the development. The equilibrium used is a solution to the basic Eqs. (18)–(24) with the time derivative of all quantities set to zero, $\mathbf{v}=0$ and $\eta=0$ (we use an ideal equilibrium). This is discussed in more detail in Ref. [4]. Since axisymmetric perturbed modes ($n=0$; see next section) are used, quasilinear equilibrium modifications are included exactly.

For numerical solution, the quantity α in Eqs. (18)–(20) is replaced in a consistent manner by

$$\alpha^* = \alpha - \left[\frac{1}{\rho}\frac{\partial}{\partial\rho}(\rho\chi_{\text{eq}})\phi - \left(\frac{\partial}{\partial\rho}\psi_{\text{eq}}\right)A\right]\bigg/R^2.$$

This replacement simplifies some of the terms involved in the solution of these equations. It also allows the rational surfaces to be identified more cleanly by placing the relevant operator in one and only one mode. This use of one mode minimizes problems with round-off errors numerically. From this point on, α^* is referred to as α.

Equations (18)–(24), together with the definitions given by Eqs. (25)–(35), give the equations that are numerically time-advanced in the computer code FAR. For incompressible calculations, Eqs. (18)–(22) are time-advanced and ω is zero in the velocity components given by Eqs. (33)–(35). Since $\partial\omega/\partial t = (\partial/\partial t)(\nabla\cdot\mathbf{V})$ must be identically zero, Eq. (23) serves as a diagnostic equation to determine the pressure. For compressible calculations, on the other hand, the full set of equations is used.

The preceding form of MHD equations is particularly useful because of the natural transition between compressible and incompressible models. It is also very useful to have direct access to the fast-wave contribution to the MHD equations (see Section 6). The form used here gives such direct access through Eq. (23) (for $W\equiv\nabla\cdot\mathbf{V}$). Thus, for modes that do not depend on the details of the fast waves, the wave motion can be damped or modified directly through Eq. (23).

3. NUMERICAL METHOD

For computations with the computer code FAR, the dependent variables (X) are separated into equilibrium (X_{eq}) and perturbed ($\tilde{X}$) parts,

$$X(\rho,\theta,\zeta) = X_{\text{eq}}(\rho,\theta) + \tilde{X}(\rho,\theta,\zeta). \tag{36}$$

The purely equilibrium terms cancel by use of the equilibrium equation, and only terms that are linear or quadratic in the perturbed quantities remain. They are expanded in Fourier series in angular variables θ and ζ [9]. Assuming up–down symmetry of the equilibrium, the perturbed quantities $\tilde{\psi}$, $\tilde{\chi}$, $\tilde{p}$, and $\tilde{\omega}$ can be expanded in cosine functions,

$$\tilde{X}(\rho,\theta,\zeta) = \sum_{m,n}\tilde{X}_{mn}(\rho)\cos(m\theta+n\zeta), \tag{37}$$

and $\tilde{\psi}$, $\tilde{\Lambda}$, and $\tilde{\alpha}$ in sine functions,

$$\tilde{X}(\rho, \theta, \zeta) = \sum_{m, n} \tilde{X}_{mn}(\rho) \sin(m\theta + n\zeta). \tag{38}$$

For incompressible calculations, p and ω are, of course, omitted.

In the radial direction (ρ), centered finite differences are used with the provision for a variable mesh spacing [9]. The equations to be time-advanced can be written symbolically as

$$\mathbf{A}\, \partial_t \mathbf{X} = \mathbf{B}\mathbf{X} + \mathbf{X}^+ \mathbf{C}\mathbf{X}, \tag{39}$$

where $\mathbf{X}$ is the vector of unknowns, $\mathbf{A}$ and $\mathbf{B}$ are two-dimensional matrices containing the linear coefficients, and $\mathbf{C}$ is a three-dimensional matrix that gives the nonlinear strength of each quadratic term. Each component of the vector is one Fourier component of the unknown evaluated at one of the grid points. The linear terms are evaluated implicitly by using a time-centered scheme that allows very large time steps to be taken for linear calculations ($\mathbf{C} \equiv 0$). As discussed in detail in Ref. [4], these very large time steps give convergence in only a few iterations. The time step then becomes a convergence parameter that can be chosen to accelerate convergence if an approximate value for the growth rate is known, as is usually the case. The nonlinear terms ($\mathbf{C} \neq 0$) are added explicitly, and nonlinear calculations must therefore be done with greatly reduced time steps sizes. The step size required for nonlinear compressible calculations is discussed later in more detail. The Fourier series of Eqs. (37) and (38) are truncated, and a finite difference representation is used in the radial coordinate ρ with a three-point, centered, uniform spatial, finite difference scheme. This three-point finite difference scheme gives a block tridiagonal matrix. Details of the procedure used to set up the blocks and the method of inverting the large matrices is contained in Refs. [4, 6]. This scheme does not allow the direct evaluation of radial third derivatives. Examination of the equation for W [Eq. (23)] shows that such terms appear linearly through $\partial J_\theta/\partial\rho$ and $\partial J_\zeta/\partial\rho$. These are handled by the technique of using auxiliary equations.

Thus, for example, the third-order equation,

$$X = \partial_\rho^3 Y, \tag{40}$$

can be written as one first-order plus one second-order equation as

$$X = \partial_\rho Z, \tag{41}$$

$$Z = \partial_\rho^2 Y. \tag{42}$$

In the compressible version of FAR, the expressions for J_ρ, J_θ, and J_ζ are treated by using auxiliary equations (an equation is added: $J_i - f(\psi, \chi) = 0$]. Two (J_θ, J_ζ) are needed to allow the third derivatives to be taken (in Eq. (23)), and the third (J_ρ) is added simply to treat all J_i's in a symmetric fashion. With the implicit scheme used in FAR [4] for linear calculations, the coding is also much simpler; if the auxiliary equations were not used, the implicit scheme would require $\partial J_i/\partial\rho$

to be evaluated analytically (and coded). This technique is also useful to impose boundary conditions on quantities like J_l since, without the dummy equation, one does not have direct access to the quantity to impose a boundary condition. This property of the technique allows the edge boundary conditions on J_l to be consistent with the boundary conditions assumed in the magnetic equations. This is discussed in Section 4.

An additional consideration is the first-order equation for α (Eq. (18)). Solving the equation as written by the implicit matrix technique leads to a grid separation problem. In the FAR code this is solved by making the transformation

$$\alpha \to \alpha + D_\alpha \frac{\partial \alpha}{\partial \rho}, \tag{43}$$

where D_α is a constant. This change transforms Eq. (18) into a second-order equation and modifies linear terms in the equations for toroidal flux (Eq. (19)) and for poloidal flux (Eq. (20)) but otherwise leaves the original set of equations unmodified. The second-order equation is desirable because the present three-point, centered numerical scheme evaluates first derivatives at a given grid point by using the function values only at adjacent grid points. This leads to grid separation. When a second derivative is evaluated, on the other hand, the values of the function at three grid points are used; use of the three values couples the grid and alleviates the problem. This "smoothing" from D_α is due to the numerical radial differencing, but tests have shown that the results are independent of D_α over a wide range.

Typically results are obtained with the code using ~300 grid points and ~10 Fourier components. This number of grid points can be too few for very small growth rates when a convergence study is needed (i.e., find the growth rate using several different grid spacings and extrapolate to zero grid spacing in some reasonable way). The above number of Fourier components can be too few for some modes. A low n ballooning mode for instance can require ~30. Typical time requirements on a CRAY II computer are a few tens of minutes for a linear result in toroidal geometry and a few tens of hours for a nonlinear calculation also in toroidal geometry.

4. Boundary Conditions and Origin Behavior

The conditions on the unknown quantities at the magnetic axis are found by requiring that none of the fields, and none of the fields obtained from them by applying standard vector operators, have singularities at the origin. As in Ref. [4], this means that, for the scalar fields (α, p, and for ω) and for the toroidal components of vector fields ($\psi = A_\zeta$, and $\phi = -\Omega_\zeta$) the (mn) harmonics must approach the origin as

$$X_{mn} = \rho^{|m|} \sum_{k=0}^{\infty} a_{2k} \rho^{2k}. \tag{44}$$

For poloidal components ($\chi = -A_\theta$ and $\Lambda = -\Omega_\theta$), origin conditions are

$$Y_{mn} = \rho^{||m|-1|} \sum_{k=0}^{\infty} a_{2k} \rho^{2k}, \tag{45}$$

with the additional constraint that, for $m \neq 0$, the leading terms of the ρ and θ components satisfy

$$(a_0)_\rho = \pm \frac{m}{|m|} (a_0)_\theta. \tag{46}$$

The plus sign is taken for a θ component with a cosine series, and the minus sign is taken when the θ component has a sine series. In FAR, the scalar fields p, α, and ω and the vector fields ψ and ϕ are taken to satisfy Eq. (44). However, as is discussed in detail in Ref. [4], α is taken to be zero at the origin. The poloidal vector fields χ and Λ are taken to satisfy Eqs. (45) and (46). It can then be seen that the gauge conditions $A_\rho = 0$ and $\Omega_\rho = 0$ imply, together with Eq. (47), that $a_0 = 0$ in Eq. (45) when $m \neq 0$. Hence, $\chi_{mn} \sim \rho^{|m|+1}$ as the origin is approached and similarly for Λ_{mn}.

A perfectly conducting wall boundary condition is imposed at the plasma edge which implies

$$B^\rho |_{\rho=a} = 0. \tag{47}$$

This is satisfied by requiring

$$m\psi_{mn} |_{\rho=a} = n\chi_{mn} |_{\rho=a}. \tag{48}$$

The edge values for ψ and χ are time-advanced by

$$\left.\frac{\partial \psi}{\partial t}\right|_{\rho=a} = \left[-\frac{F_{\text{eq}}}{qR^2} \left(\frac{\partial}{\partial \theta} - q \frac{\partial}{\partial \zeta} \right) \phi - \frac{\partial \alpha}{\partial \zeta} \right]_{\rho=a} \tag{49}$$

and

$$\left.\frac{\partial \chi}{\partial t}\right|_{\rho=a} = \left[-\frac{F_{\text{eq}}}{qR^2} \left(\frac{\partial}{\partial \theta} - q \frac{\partial}{\partial \zeta} \right) \Lambda - \frac{\partial \alpha}{\partial \theta} \right]_{\rho=a}. \tag{50}$$

The solutions of Eqs. (49) and (50) are consistent with Eq. (48) provided that $m\phi_{m,n} |_{\rho=a} = n\Lambda_{m,n} |_{\rho=a}$. Equations (49) and (50) are simply Eqs. (19) and (20) linearized and with $\tilde{J}_\zeta |_{\rho=a} = \tilde{J}_\theta |_{\rho=a} = 0$ (as required by a conducting wall). An additional boundary condition implied by the perfectly conducting wall is

$$V^\rho |_{\rho=a} = 0. \tag{51}$$

For incompressible calculations, Eq. (51) is satisfied in the same manner as Eq. (47) is, namely, by requiring

$$m\phi_{mn} |_{\rho=a} = n\Lambda_{mn} |_{\rho=a}. \tag{52}$$

For compressible calculations, the additional constraint (see Eq. (33))

$$\left(g^{\rho\rho}\frac{\partial\omega}{\partial\rho}+g^{\rho\theta}\frac{1}{\rho}\frac{\partial\omega}{\partial\theta}\right)_{\rho=a}=0 \tag{53}$$

is needed. This separation of the boundary condition, $V^{\rho}\,|_{\rho=a}=0$, into two parts (Eqs. (52) and (53)) is permitted because of the gauge invariance of the problem. Equations (49), (50), and (53) give boundary conditions for ψ, χ, and ω that are highly coupled (the boundary value for a given m, n depends on all other m, n pairs).

For a consistent solution to the problem, the number of boundary values imposed must be the same as the order of the equation. In Table I, the orders of

TABLE I

Boundary Values

	Linear					
	Incompressible			Compressible		
Variable	Order	Origin	Edge	Order	Origin	Edge
ψ	2	ρ^{m}	Time advanced	3	ρ^{m}	Time advanced; $J_{\zeta}\|_{a}=0$
χ	2	ρ^{m+1}	Time advanced	3	ρ^{m+1}	Time advanced; $J_{\theta}\|_{a}=0$
α	2	0	Extrapolated	1	0	Extrapolated
Λ	2	ρ^{m+1}; $\partial_{\rho}\Lambda=0$	$n\Lambda\|_{a}=m\phi\|_{a}$	2	ρ^{m+1}; $\partial_{\rho}\Lambda=0$	$n\Lambda\|_{a}=m\phi\|_{a}$
ϕ	2	ρ^{m}	$n\Lambda\|_{a}=m\phi\|_{a}$	2	ρ^{m}	$n\Lambda\|_{a}=m\phi\|_{a}$
ω				2	ρ^{m}	$[g^{\rho\rho}\partial_{\rho}\omega+g^{\rho\theta}(1/\rho)\partial_{\theta}\omega]_{a}=0$
p				2	ρ^{m}	0

	Nonlinear[a]			
	Incompressible		Compressible	
Variable	Order	Values	Order	Values
ψ	1	$J^{\zeta}\|_{a}=0$	0	
χ	1	$J^{\theta}\|_{a}=0$	0	
α	0		0	
Λ	1	$U^{\theta}\|_{a}=0$	1	$U^{\theta}\|_{a}=0$
ϕ	1	$U^{\zeta}\|_{a}=0$	1	$U^{\zeta}\|_{a}=0$
ω			1	$V^{2}\|_{a}=0$
p				

[a] Order and boundary values *in addition* to those for the linear problem.

the equations to be solved are given, together with the boundary values imposed. These boundary values are limited by three constraints: (1) the order of the equation for each variable (as just mentioned), (2) the perfectly conducting wall boundary condition that specifies the physics at the boundary, and (3) the time independence of V^ρ and B^ρ at the boundary [8]. The last condition results because the normal components of the velocity and the magnetic field must be zero at the wall independent of time and thus $\partial_t V^\rho |_{\rho=a} = \partial_t B^\rho |_{\rho=a} = 0$. Since the problem is formulated in terms of magnetic fluxes and velocity stream functions, one does not have direct access to V^ρ and B^ρ.

It can be verified by direct calculation that, for the linear problem, the boundary values shown in Table I guarantee the time independence of B^ρ and V^ρ if $\partial_\rho p_{\mathrm{eq}} |_{\rho=a} = 0$. Nonlinearly, only instabilities that have a small perturbation near the wall can be studied, which provides no additional physics limitation on this fixed-boundary conducting wall model. The implementation of these boundary conditions requires that the solution be formed from a combination of the homogeneous and inhomogeneous solutions to the discrete matrix form. Full details of this are given in Ref. [4].

Table I shows that the order of the equations and the number of equations increase when compressibility is included. Since the incompressible equations are a particular limit of the fully compressible set $(\Gamma = \infty)$, their boundary conditions must be a subset of those for the fully compressible equations. Thus, for instance, the change from second to third order in ψ and χ as compressible terms are included requires two additional boundary values. For consistency, these values are imposed on $J_\zeta |_a$ and $J_\theta |_a$ through the new auxiliary equations. This imposition, in turn, is consistent with the assumption used in time-advancing the boundary values for ψ and χ in the incompressible case. It would be difficult to impose the new boundary values in any other manner because they must be included in such a way that they are not seen by the incompressible problem. If they are seen, the problem would be overspecified. Since J_ζ and J_θ are not explicitly required incompressibly, they satisfy this consideration. They are required compressibly because a third-order derivative must be taken (see earlier discussion). The need for the imposition of two boundary conditions for Λ at the origin is discussed in detail in Ref. [4] and thus is not repeated here. The imposition of boundary values required by the nonlinear terms must also be done in a manner that is consistent with the linear problem. That is, the values must be imposed in such a way that, when a linear calculation is done, it is not overspecified. All the above conditions are satisfied by the boundary values shown in Table I.

5. Time Step for Compressible Calculations

As is well known, the addition of compressibility adds the fast Alfvén time scale to the problem [11–13]. This shorter time scale can require a much smaller time equations and the shorter time step requirement would both, of course, increase the computational cost of the problem. For linear calculations, the implicit method is unconditionally stable, and this stability alleviates the need for the smaller time step. Just as described in Ref. [4], for an incompressible problem, the value of the time step may be chosen to provide convergence of the mode in a few steps, independent of the very small time scale behavior. (When the time step is chosen in this way, it is no longer a time step but serves as a convergence parameter.) This behavior is illustrated for the compressible problem in Fig. 1. The radial and poloidal velocity are shown, together with the compressible quantities ω and $W = \nabla \cdot \mathbf{V}$. They are displayed at various times during the evolution for a small time step that follows the short-time-scale behavior ($\Delta t/\tau_{HP} = 0.5$) and for a large time step ($\Delta t/\tau_{HP} = 5.0$) for which the calculation cannot resolve very-short-time-scale behavior. The time dependence with the small time step is shown on the left, and that with the large time step is shown on the right. The quantities displayed are very different at times before the mode became a converged eigenfunction, but they are the same at the final time shown. The eigenvalues found by the methods of Ref. [4] are absolutely identical. Thus, the implicit methods described here bypass the requirement of the small time step in solving the linear problem. The implicit nature of the numerical algorithm allows the large time step. The short-time-scale behavior, which is omitted, is irrelevant to the linear eigenfunction since the eigenfunction and eigenvalue are independent of the time step for the values chosen.

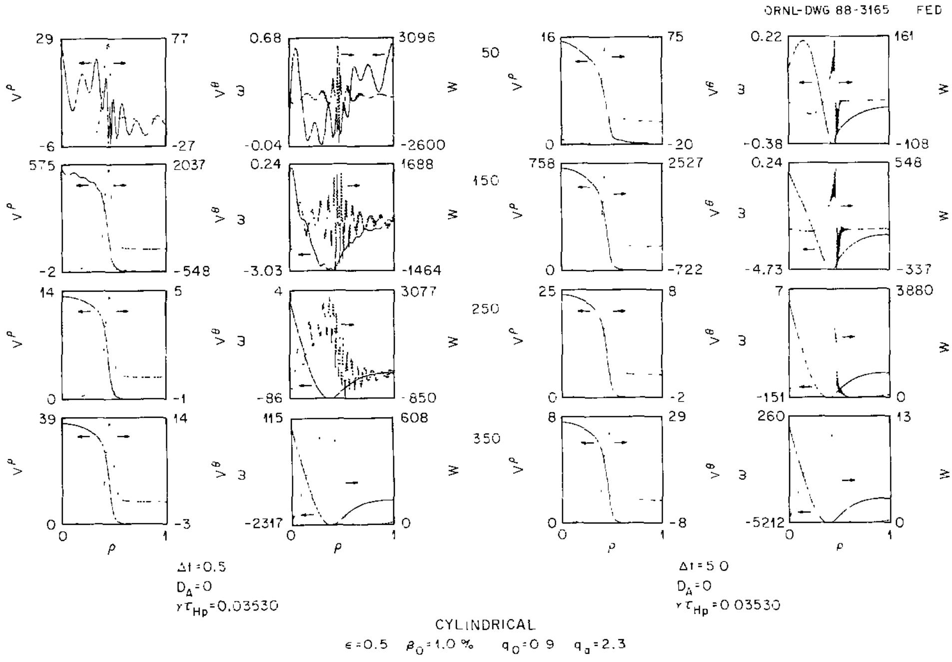

FIG. 1. Comparison between linear time evaluations with $\Delta t = 0.5$ and $\Delta t = 5$ ($D_A = 0$). The time is shown (in units of τ_{Hp}) in the center of the figure. W and ω are defined in the text.

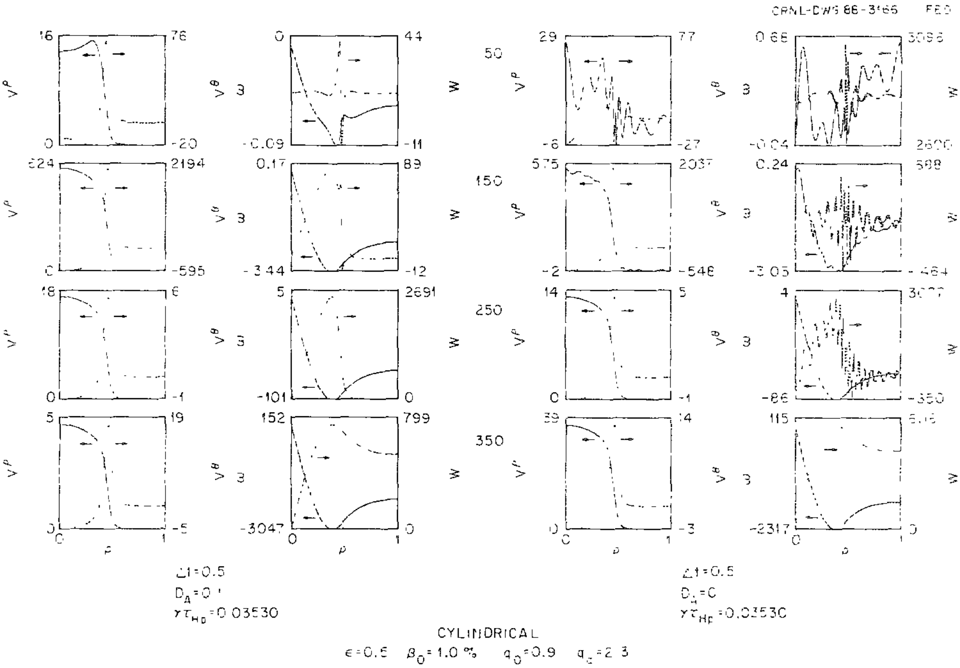

FIG. 2. Comparison between linear time evolutions with $D_A = 0.1$ and $D_A = 0$ ($\Delta t = 0.5$). The time is shown (in units of τ_{Hp} in the center of the figure. W and ω are defined in the text.

For nonlinear calculations, D_A is made nonzero (see Eq. (23)). The term this introduces has the form of a viscosity that serves to damp the short-wavelength wave motion introduced when compressibility is included. A comparison is made between linear calculations done with $D_A = 0$ and $D_A = 0.1$ in Fig. 2. The damping of the wave notion is clear. Note that the linear eigenfunctions and growth rates are identical after a converged eigenfunction is reached. The linear growth rate is shown in Fig. 3 as a function of D_A. The growth rate corresponding to $D_A = 10^{-3}$ on the extreme left of the graph (labeled $\gamma_C \tau_{HP}$) is identical to that for $D_A = 0$. For values of $D_A \leqslant 0.1$, the growth of the mode and the structure of the linear mode are unaffected. For the nonlinear calculation shown later using the same equilibrium, $D_A = 0.1$ was used. The asymptotic growth rate (labeled $\gamma_I \tau_{HP}$) is identical to the incompressible growth rate. The structure of the mode also undergoes a transition from the compressible mode for $D_A \lesssim 0.1$ to the incompressible mode for $D_A \gtrsim 10^3$. As can be seen from examination of Eq. (23), large values of D_A yield a result in which W ($= \nabla \cdot \mathbf{V}$) is completely damped, giving an incompressible mode. Thus, using a moderate value for D_A in the manner described leaves the linear eigenfunction unchanged in structure (see the bottom of Fig. 2) and in growth (the linear growth rate is the same). If too large a value of D_A is used, however, an incompressible linear mode evolves. This technique is somewhat similar to semi-implicit techniques used by many [12, 13]. The semi-implicit techniques damp the

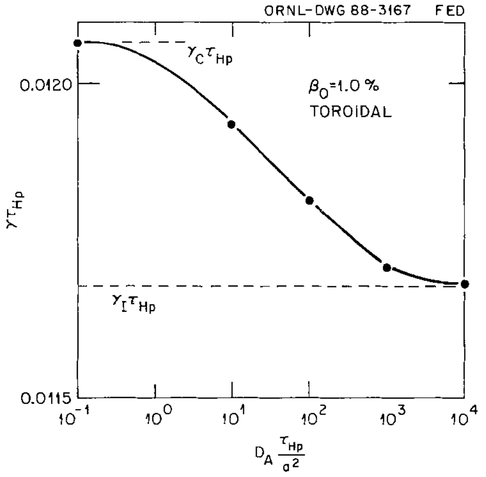

FIG. 3. Growth rate vs D_A.

Alfvén waves by effectively canceling the driving term for these waves. They do so with a nondiffusive method. The method used here is, of course, diffusive but leaves the linear eigenfunction unchanged.

6. RESULTS

The results presented here are of two different types. The first is a comparison with previous codes, which serves to validate the FAR code. Codes that evaluate precisely the same physics as a new code are usually unavailable (if they were readily available the code would not be written!). Thus, it is necessary to validate a new code by comparing it with others that are identical only in some limit. The code FAR, the subject of this paper, solves the complete set of MHD equations in toroidal geometry. However, one set of comparisons given here is with the fully compressible, partially implicit, cylindrical-geometry code CYL [14], for both linear and nonlinear calculations. For the CYL comparison, identical cylindrical equilibria were used in both codes.

Results are also shown for a comparison with the linear, ideal, toroidal geometry code ERATO [3]. For the comparisons shown, FAR is run ideally with the resistive terms turned off. However, many ideal-mode studies have been done by setting S sufficiently large to make the resistive terms negligible. Thus, the ideal results can be regarded as either purely ideal calculations or as a limit in which S is made very large.

The second type of results shown is a comparison between compressible and incompressible calculations. This comparison is shown to illustrate the capabilities of the code. A paper describing a detailed study of the effects of compressibility will be published in the near future. All the results presented here have been checked for convergence with respect to the radial mesh and poloidal spectrum (for toroidal calculations). Extensive details of these types of convergence studies are given in Ref. [4] and thus are not be repeated here.

A comparison between FAR and CYL results is shown for a linear calculation in Fig. 4. Linear compressible terms were kept in both codes with a cylindrical equilibrium. The safety factor profile used was

$$q(\rho) = q_0 \left[1 + \left(\frac{\rho}{\rho_0} \right)^{2\lambda} \right]^{1/\lambda},$$

with $q_0 = 0.9$, $\lambda = 2$, and $\rho_0 = 0.6521$ [4]. A pressure profile given by

$$p(\psi) = p_0 \left[1 - \left(\frac{\psi}{\psi_a} \right)^2 \right],$$

where ψ is the poloidal magnetic flux and ψ_a is its value at the plasma edge. The constant p_0 was chosen to give $\beta_0 = 1.0\%$ at the magnetic axis. The equilibrium

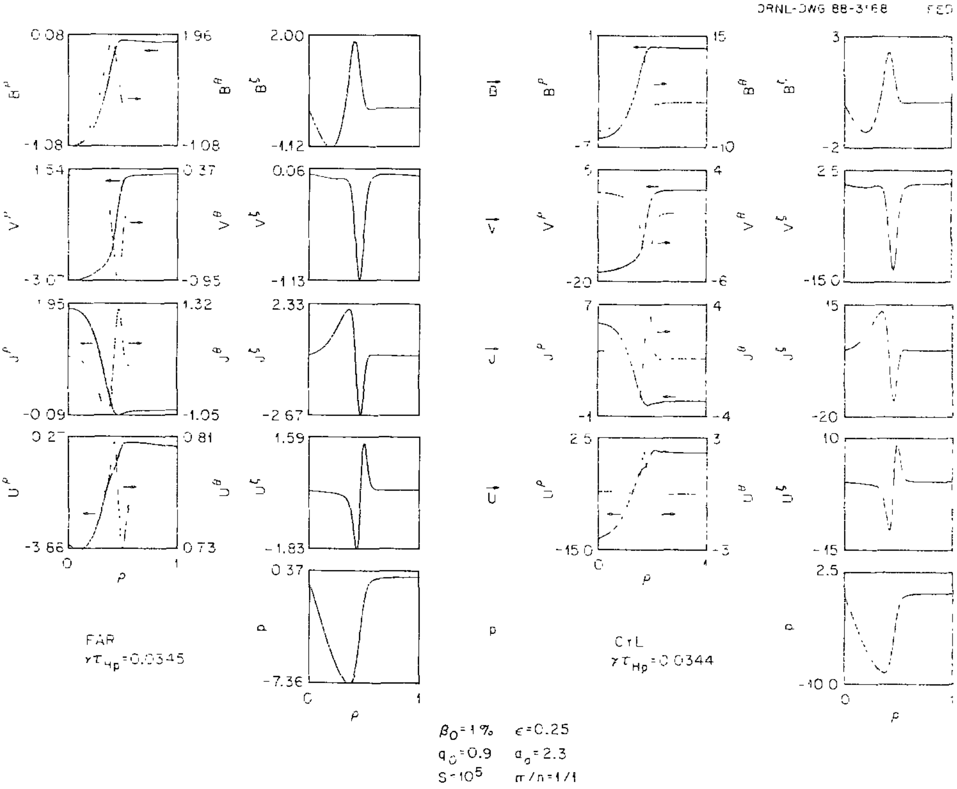

FIG. 4. Eigenfunction components from FAR and CYL for identical equilibrium input for an $m, n = 1/1$ mode.

represented a tokamak plasma with an aspect ratio ($\varepsilon_L = 2\pi a/L$, where a and L are the radius and length of the cylinder, respectively) of 4.0 and a circular cross section. Shown at the left in Fig. 4 is the eigenfunction given by FAR; on the right is shown the eigenfunction from CYL, with the three components for (from top to bottom) the magnetic field, velocity, current density, and vorticity displayed. The mode is a resistive internal kink. At the bottom is the pressure from each code with the linear growth rate. As can be seen, both the eigenfunction and the growth rate for FAR and CYL are virtually identical. As detailed earlier, FAR uses a formulation in terms of magnetic fluxes and stream functions, whereas CYL solves the primitive magnetic field and velocity equations. FAR must satisfy the conducting wall boundary conditions on the magnetic and velocity fields through the fluxes and stream functions, whereas in CYL the relevant boundary values can be [illegible] radically different in their approach to solving the same equations. In Fig. 5, another comparison between the codes is shown for larger m, n ($m/n = 7/7$) and for

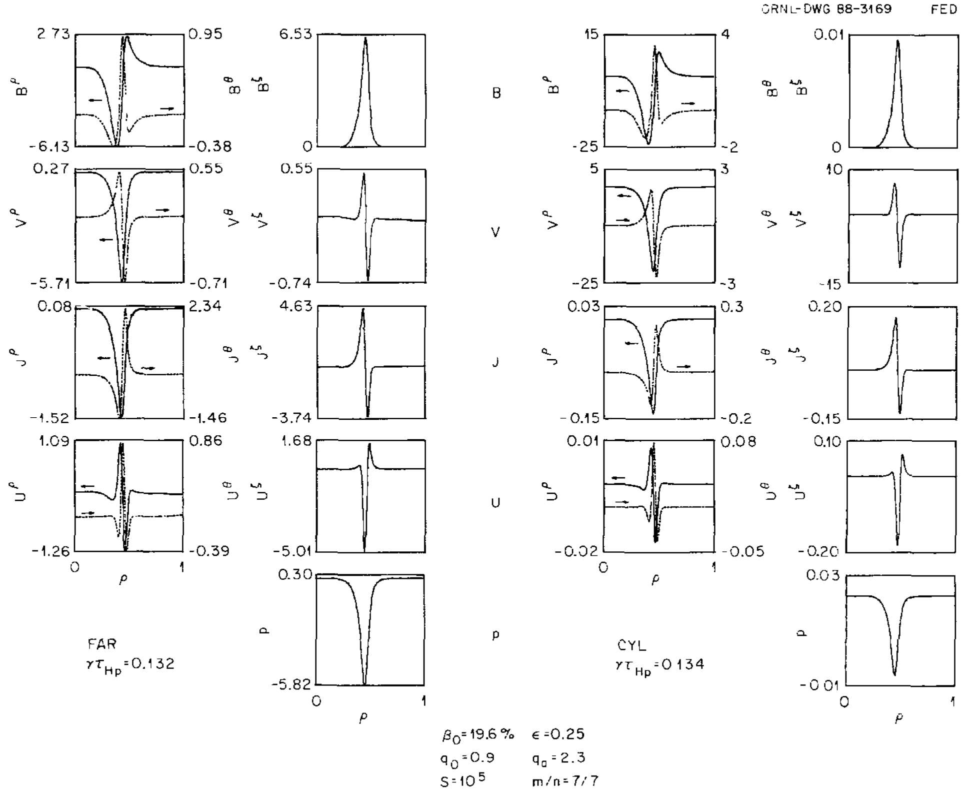

FIG. 5. Eigenfunction components from FAR and CYL for identical equilibrium input for an $m/n = 7/7$ mode.

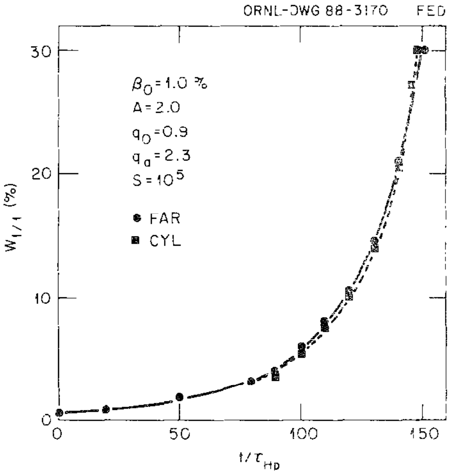

FIG. 6. Comparison between the FAR and CYL, $m/n = 1/1$ magnetic island widths ($W_{1/1}$) as a function of time.

higher β ($\beta_0 = 19.6\%$). The other equilibrium parameters were identical to those of Fig. 4. Again, the eigenfunctions and growth rates are in very good agreement.

A comparison between the nonlinear evolution calculated with FAR and CYL for a resistive kink is shown in Fig. 6. Compressible effects are included. The equilibrium is cylindrical and has the same parameters as those for the $\beta_0 = 1\%$ linear comparison (Fig. 4) except for a smaller aspect ratio ($A = 2.0$). Shown is the $m/n = 1/1$ magnetic island width vs time. The agreement is quite good. Of course, the early growth shows the linear behavior of the two codes.

Figure 7 shows a comparison between the linear growth rates at various inverse aspect ratios, calculated with the ERATO and FAR codes. The equilibrium used is

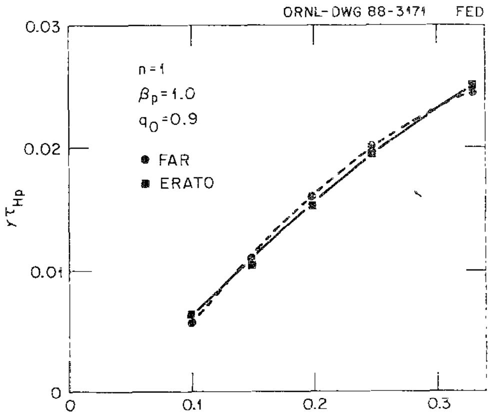

FIG. 7. Growth rates from FAR and ERATO vs the inverse aspect ratio (ϵ).

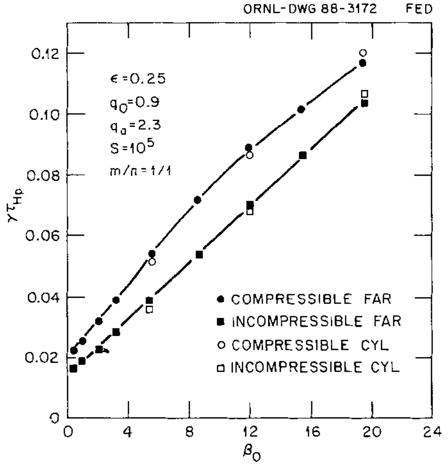

FIG. 8. Comparison between compressible and incompressible cylindrical growth rates from FAR and CYL.

specified by $FF'=0$ (where F denotes the major radius times the toroidal magnetic field and F' denotes the derivative with respect to the poloidal flux), pressure proportional to the square of the poloidal flux, $\beta_p=1.0$, and $q_0=0.9$. The mode is an ideal internal kink. As can be noted, the agreement is excellent.

Let us now consider the effect of compressibility on the internal kink (Fig. 8). The growth rate is shown as a function of β_0. The equilibrium parameters are identical to those given earlier, with $A=4.0$ and p_0 adjusted to give the desired β_0. Compressible and incompressible growth rates were found as detailed earlier. Comparisons are shown between growth rates found by use of CYL and FAR. As for the CYL–FAR comparison shown earlier, the agreement is quite good for all values of β_0 and for both compressible and incompressible calculations.

A nonlinear comparison between compressible and incompressible calculations for a resistive kink in toroidal geometry is shown in Fig. 9. The equilibrium used was found with parameters identical to those for the $\beta_0=1\%$, $A=4.0$ case discussed earlier except that now the equilibrium has full toroidal effects. Shown is the $m/n=1/1$ island width, $W_{1,1}$, vs time. A complete reconnection has occurred when $W_{1,1}=90\%$. The process seen corresponds to the classical Kadomtsev reconnection when a $m/n=1/1$ resistive kink leads to the formation of a magnetic island that grows until it fills the interior of the original $q=1.0$ surface. This process has flattened the q profile inside the original $q=1.0$ surface so that $q=1.0$ is no longer in the plasma. Through this relaxation the mode is stabilized. The reconnection time is slightly shorter for the compressible evolution than for the incompressible. This is due, for the most part, to the slight difference in linear growth rate. Thus, the gross behavior of the process is very similar for both compressible and incompressible evolutions.

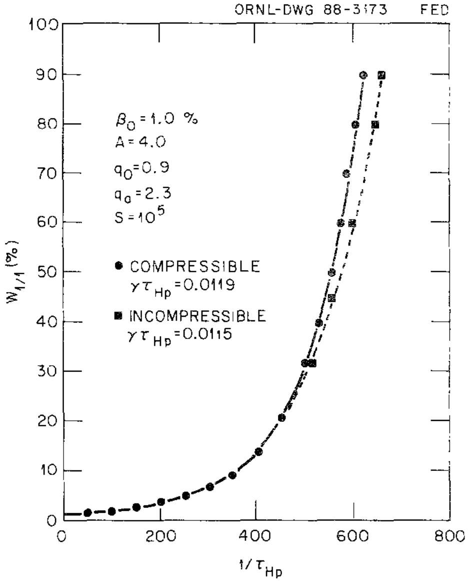

FIG. 9. Magnetic island width ($W_{1\,1}$) vs time from FAR calculations with compressible and incompressible equations. Both are fully toroidal.

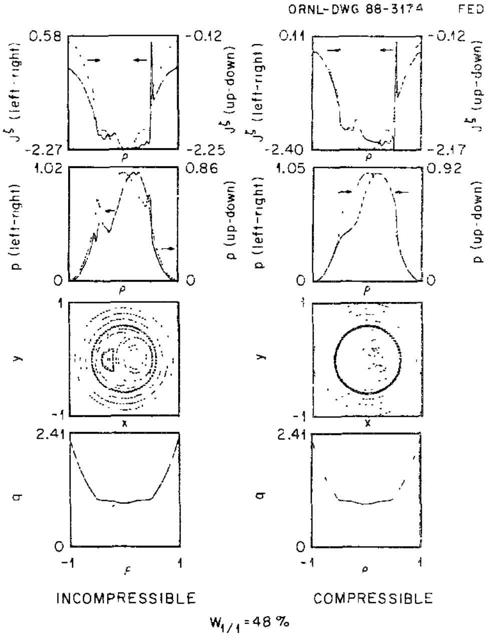

FIG. 10. Comparison of the toroidal current density (J^ζ), the pressure (p), the $m/n = 1/1$ helical flux contours, and the safety factor from the nonlinear toroidal FAR calculations with compressible and incompressible equations. This comparison is made when the island width is 48 % of the minort radius.

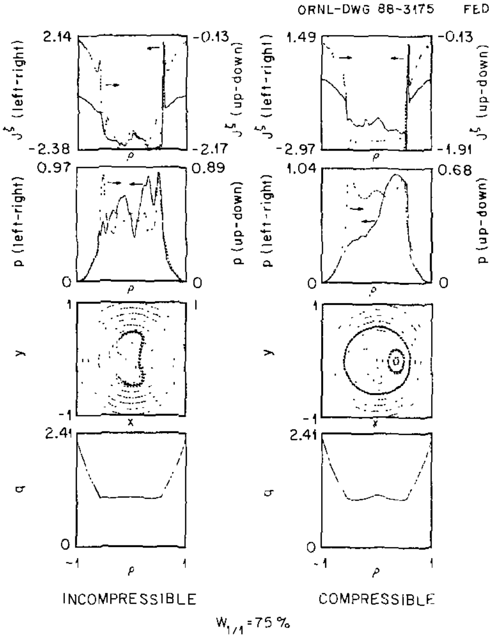

FIG. 11. Comparison of the toroidal current density (J^ζ), the pressure (p), the $m/n = 1/1$ helical flux contours, and the safety factor from the nonlinear toroidal FAR calculations with compressible and incompressible equations. This comparison is made when the island width is 75% of the minor radius.

The details of the nonlinear evolution are shown in Figs. 10 and 11. The current density profiles, pressure profiles, $m/n = 1/1$ helical flux contours, and safety factor profiles are shown in Fig. 10 at the time when the magnetic island width is 48% of the length of the minor radius. The characteristic spike in the current density has developed with an accompanying flattening of the profile over the region covered by the magnetic island. The current density profile for the compressible case is very similar to that for the incompressible case. This is also true of the gross features of the pressure profiles. The details of the pressure profiles are quite different, however. For the calculations including compressibility effects, the pressure profile decreases monotonically through the island region; in the incompressible limit, however, the pressure profile exhibits a secondary maximum in this region. The resulting pressure profile for the calculation in the incompressible limit exhibits a great deal more structure than in the compressible case. The reason for these differences can be seen in the helical flux contour shown directly below the pressure profiles. The magnetic island for the incompressible case is much deeper, as shown by the large number of contours in the island region. The island for the compressible case, on the other hand, is very shallow, with no contours (indicating that the depth is less than the difference between the values of the flux on each contour). There is also more structure in the incompressible case, indicating the contribution is higher m values. Thus, the pressure, which is an approximate flux surface quantity, shows both the effect of the deeper island by having a secondary peak and the effect of the increased structure in the flux behavior. The safety factor profiles are quite similar, however, showing the flattening that results as the plasma evolves toward a state in which the $q = 1$ surface is removed from the plasma. Thus, there are large differences in the details of the dynamical evolution for the two cases considered. The features just noted in Fig. 10 (when the island width was 48 %) are also present but enhanced in Fig. 11 for an island width of 75%. A well-developed secondary peak in the pressure profile is now evident for the incompressible case, whereas the pressure decreases monotonically in the compressible calculation. The pressure still exhibits much more detailed structure incompressibly than compressibly. Field line plots are shown in Fig. 12 for the same island widths as in Figs. 10 and 11 ($W_{1/1} = 48\,\%$ and $W_{1,1} = 72\,\%$). The field line plots were generated by following a field line around the torus many times, leaving a point as a given poloidal plane is passed. They generally exhibit the same structure as the $m/n = 1/1$ helical flux contours. The closed curves on the field line plots, however, do not show all equally [illegible]

Fig. 13 for the equilibrium whose nonlinear evolution is shown in Figs. 10–12. The modes are very similar except for the toroidal velocity, which is very different, particularly in the region inside the $q = 1.0$ surface.

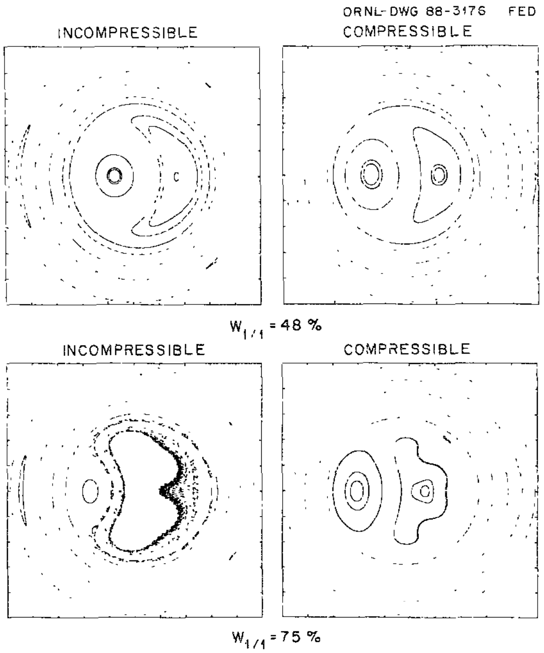

FIG. 12. Field line plots at the same points in the nonlinear evolution as shown in Figs 10 and 11.

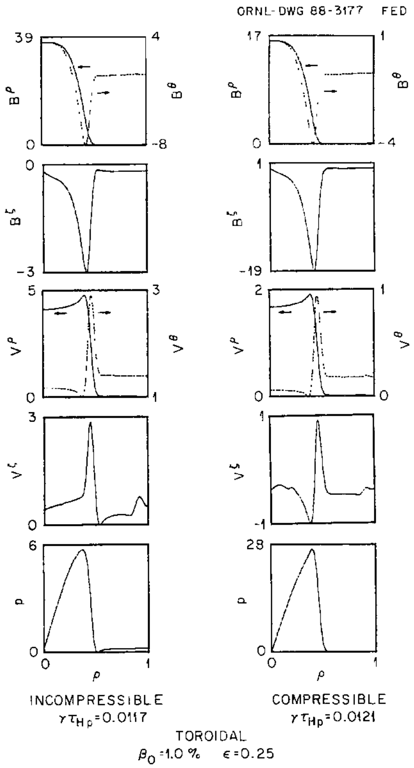

FIG. 13. Linear eigenfunctions for the same equilibrium for which nonlinear results are shown in Figs. 10–12.

7. DISCUSSION AND CONCLUSIONS

The computer code FAR, which performs linear or nonlinear and resistive or ideal MHD calculations in full toroidal geometry with no ordering assumptions, has been constructed and validated. The code can be used for either compressible or incompressible calculations. It uses a fully implicit algorithm for linear calculations. This permits very efficient linear calculations because a very large step size can be used which permits fast convergence to the linear eigenfunction. When a systematic parameter scan is made (so that a good guess for the growth rate is known), a few "time" steps are sufficient to give converged linear eigenfunctions.

For nonlinear calculations, the nonlinear terms are treated explicitly, which makes the time step requirement essentially that of an explicit code. In the nonlinear compressible case, however, the short-wavelength wave motion introduced by the compressibility can be damped without altering the linear behavior. Therefore, the time step required for nonlinear compressible calculations is nearly the same as that for incompressible calculations.

REFERENCES

1. A. Y. AYDEMIR, *Phys. Rev. Lett.* **59** (1987), 649; W. PARK AND D. A. MONTICELLO, Paper 1D20, "Sherwood Meeting, Gatlinburg, TN, 1988"; E. UCHIMOTO, Z. CHANG, J. D. CALLEN, AND S. C. PRAGER, Paper 2D18, "Sherwood Meeting, Gatlinburg, TN, 1988."
2. H. R. STRAUSS, *Phys. Fluids* **20**, 1354 (1977); J. A. HOLMES, B. A. CARRERAS, H. R. HICKS, V. E. LYNCH, AND K. E. ROTHE, *Phys. Fluids* **25**, 800 (1982).
3. R. GRUBER, F. TROYON, D. BERGER, L. C. BERNARD, S. ROUSSET, R. SCHREIBER, W. KERNER, W. SCHNEIDER, AND K. V. ROBERTS, *Comput. Phys. Commun.* **21**, 323 (1981); R. C. GRIMM, R. L. DEWAR, AND J. MANICKAM, *J. Comput. Phys.* **49**, 94 (1983).
4. L. A. CHARLTON, J. A. HOLMES, H. R. HICKS, V. E. LYNCH, AND B. A. CARRERAS, *J. Comput. Phys.* **63**, 107 (1986).
5. R. G. STORER, *J. Comput. Phys.* **66**, 294 (1986).
6. J. A HOLMES, L. A. CHARLTON, B. A. CARRERAS, AND V. E. LYNCH, in *Proceedings, 12th Conference on the Numerical Simulation of Plasmas, San Francisco, 1987.*
7. R. C. GRIMM, J. M. GREENE, AND J. L. JOHNSON, in *Methods in Computational Physics, Vol. 16*, (Academic Press, New York, 1976), p. 253.
8. V. E. LYNCH, B. A. CARRERAS, H. R. HICKS, J. A. HOLMES, AND L. GARCIA, *Comput. Phys. Commun.* **24**, 465 (1981).
9. H. R. HICKS, B. A. CARRERAS, J. A. HOLMES, D. K. LEE, AND B V. WADDELL, *J. Comput. Phys.* **44**, 46 (1981).
10. The author acknowledges useful conversations with D. Monticello of Princeton Plasma Physics Laboratory concerning this point.
11. S. C. JARDIN, Princeton Plasma Physics Laboratory Report PPPL-2059, 1984 (unpublished).
12. D. S. HARNED AND D. D. SCHNACK, *J. Comput. Phys.* **65**, 57 (1986).
13. D. D. SCHNACK, D. C. BARNES, Z. MIKIC, D. S. HARNED, AND E. J. CARAMANA, *J. Comput. Phys.* **70**, 330 (1987).
14. J. A. HOLMES, B. A. CARRERAS, T. C. HENDER, H. R. HICKS, V. E. LYNCH, AND B. F. MASDEN, *Phys. Fluids* **26**, 2569 (1983).